4 Readout chambers

The ALICE TRD detector is subdivided into 540 individual detector modules, as described in Chapters 1 and 2. Their task is to identify electrons by their larger energy deposition due to transition radiation and their larger specific energy loss, combined with charged particle tracking capability [1]. Each of these detector modules is a full TR detector in itself, containing a radiator and a readout chamber. The readout chamber contains a conversion and drift gas volume and a conventional wire amplification region with cathode pad readout. While the TRD readout chambers are not very demanding in terms of resolution and operational conditions, the size and number is considerable. In addition, a low mass design of the readout chambers is mandatory to reduce the load of background to subsequent TRD modules and other ALICE detectors. Therefore, apart from the required performance in terms of electron ID and position resolution, emphasis was put on mechanical reliability at minimal radiation length, combined with technical simplicity.

In the following, we describe the concept for the readout chambers and demonstrate how the technical solution is adapted to the requirements.

4.1 Choice of gas

The baseline gas mixture for the ALICE TRD is 85% Xe and 15% CO_2. The need of a high X-ray photoabsorption probability rules out any of the lower mass noble gases as major component, as demonstrated in Fig. 4.1. For a typical TR photon energy of 10 keV, the absorption length in Xenon is 1 cm.

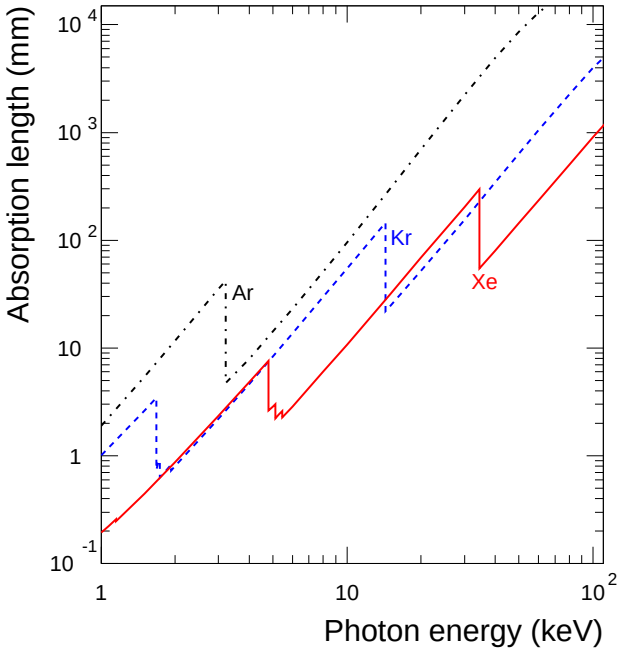

Figure 4.1: X-ray absorption length in different noble gases.

The use of CO_2 as quencher is attractive because it is nonflammable, in contrast to many organic gases. In addition, organic molecules contain hydrogen, which causes additional background from energetic knock-on protons. Since the field of the L3 magnet is perpendicular to the electric drift field of the readout chambers, also $\vec{E}\times\vec{B}$-effects have to be considered. With respect to this, the use of a 'cool' component, such as CO_2, turns out to be advantageous.

4.1.1 Drift velocity and diffusion

We have chosen a drift velocity of 1.5 cm/μs, resulting in a total drift time of 2 μs over the maximum drift distance of 3 cm. Figure 4.2 (left) shows GARFIELD/MAGBOLTZ [2,3] calculations of the drift velocity for different gas mixtures as function of the electric drift field. The drift field required in Xe,CO_2 (15%) is 700 V/cm, fixing the potential on the drift electrode to -2.1 kV. These calculations are consistent with our prototype measurements (see Chapter 14).

At this drift voltage, the longitudinal and transverse diffusion coefficients are $D_L = 250\ \mu\text{m}/\sqrt{\text{cm}}$ and $D_T = 180\ \mu\text{m}/\sqrt{\text{cm}}$ (Fig. 4.2, right panel). Due to the short drift distance of 3 cm, the maximum spread of an initially point-like charge cloud is 300-500 μm only. Therefore, the impact of diffusion on pulse shape and position resolution is negligible. It should be noted that we found no significant dependence of the drift velocity and the diffusion coefficients on the magnetic field up to B=0.6 T.

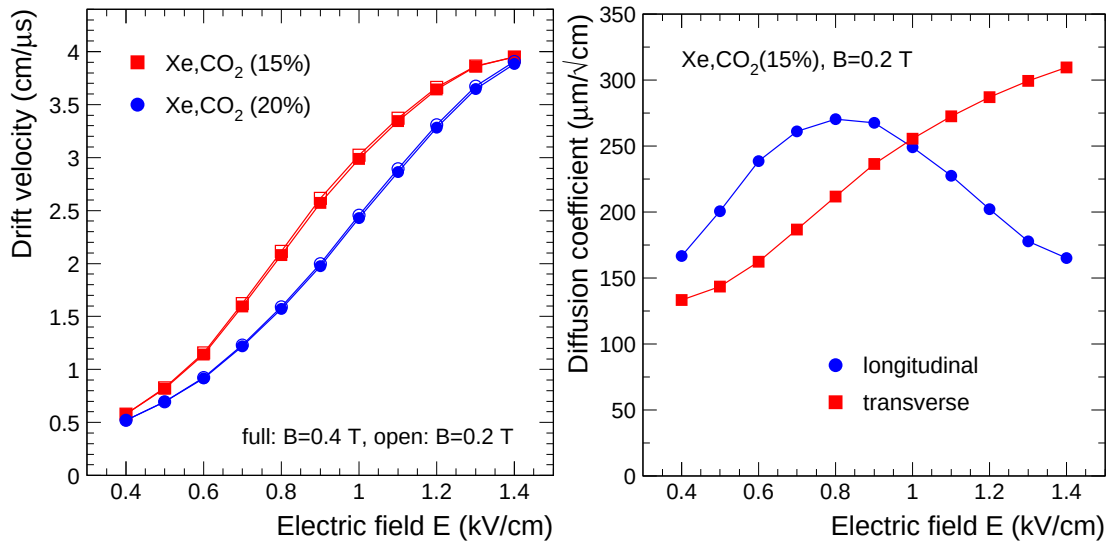

Figure 4.2: GARFIELD/MAGBOLTZ calculations of the drift velocity (left) and diffusion coefficients (right) as function of the electric drift field.

4.1.2 Lorentz angle

The ALICE TRD is operated inside the field of the L3 magnet (B_{max}=0.5 T) which is perpendicular to the electric drift field. This forces the drifting electrons on a trajectory which is inclined with respect to the electric field (see Fig. 4.3).

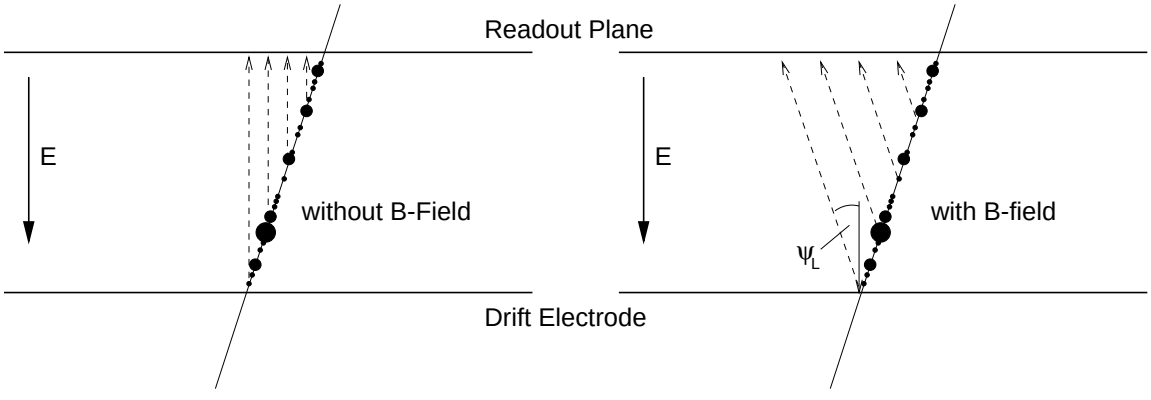

Figure 4.3: Drift path of electrons without (left) and with (right) magnetic field.

The so-called Lorentz angle ψ_L between $\vec{v}_D$ and $\vec{E}$ depends on the strength of $\vec{E}$ and $\vec{B}$ and the gas properties. It can be expressed by:

$$\tan\psi_L = \omega\tau. \tag{4.1}$$

The cyclotron frequency ω depends on B while τ is the mean time interval between two collisions of the electron in the gas, connected with the electron mobility μ:

$$\omega = e/m \cdot B, \tag{4.2}$$
$$\mu = e/m \cdot \tau. \tag{4.3}$$

Given a precise knowledge of $\vec{E}$ and $\vec{B}$, the displacement of the arriving electron with respect to its creation point is well determined and can be corrected for. However, the Lorentz angle leads on average to a deterioration of the position resolution because it enhances correlations between adjacent time bins, originating from Landau fluctuations and the finite width of the single electron response function in time direction (see Section 4.5). A minimization of the Lorentz angle is therefore desirable.

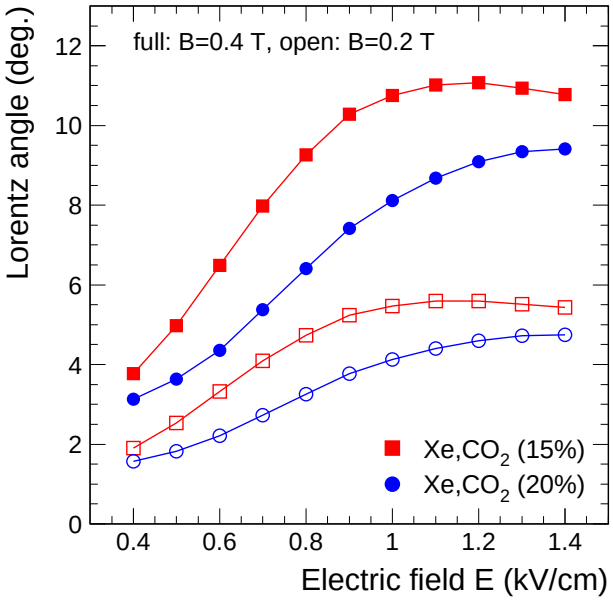

Figure 4.4: GARFIELD/MAGBOLTZ calculations of the Lorentz angle as function of the electric field for different Xe mixtures and magnetic field strengths.

The Lorentz angle as function of the drift field for different magnetic field strengths is shown in Fig. 4.4. At nominal operating conditions (E=700 V/cm, B=0.4 T), the Lorentz angle is 8° in Xe,CO_2 (15%) . Clearly, the Lorentz angle could be decreased by reducing E. On the other hand, the resulting lower drift velocity would lead to a limitation of the trigger performance (see Chapter 6). Also the addition of more CO_2 looks attractive. This would, however, tighten the requirements on the gas purity, as outlined below (see also Chapter 8).

4.1.3 Electron attachment

On their way to the amplification region, drifting electrons can be absorbed by electronegative impurities, mainly O_2. The signal loss due to this electron attachment for a given total pressure p and O_2 partial pressure $p(O_2)$ follows an exponential behaviour, depending on the drift time t_{drift}:

$$N(t_{drift}) = N(0) \cdot \exp(-p \cdot p(O_2) \cdot C_{att} \cdot t_{drift}). \tag{4.4}$$

The attachment coefficient C_{att} depends on the gas mixture. It turns out to be particularly large for gas mixtures containing CO_2 because of its large number of low-lying excitation levels. In Fig. 4.5 the attachment coefficient is shown as function of the electric drift field for different Ar mixtures and for Xe,CO_2 (15%) . Similar results have been obtained for Ne mixtures containing CO_2 [4, 5]. A measurement of the signal attenuation at different oxygen contamination levels in Xe,CO_2 (15%) was performed with the TRD prototype (see Chapter 14). The resulting attachment coefficient C_{att}=400 atm$^{-2}\mu$s^{-1} leads to a signal attenuation of less than 10% after the maximum drift time of 2 μs, for an O_2 contamination of 100 ppm.

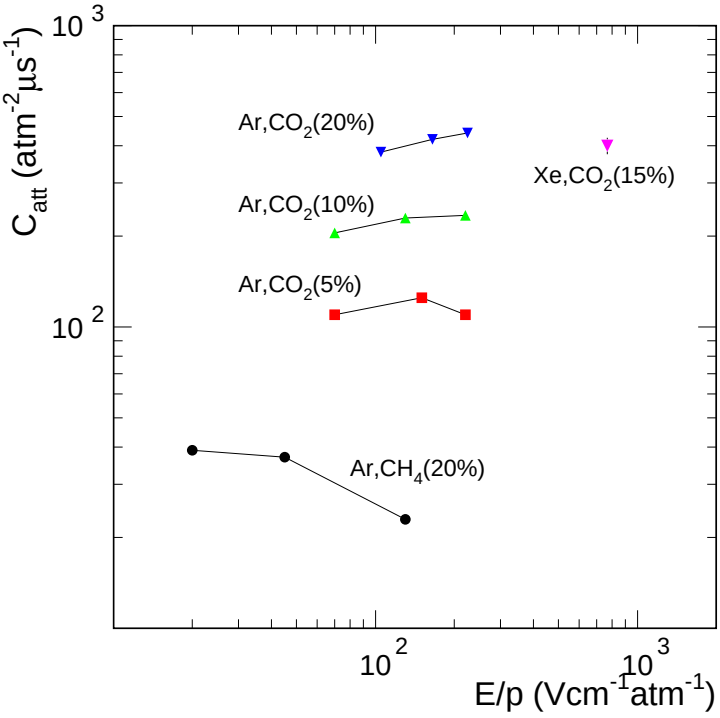

Figure 4.5: Electron attachment coefficient as function of the electric drift field and for different Ar mixtures [6] and for Xe,CO_2 (15%) .

4.2 Mechanical structure

Figure 4.6 shows a cross section through a TRD detector module. The walls of the drift box are made of fibreglass-epoxy and reinforced by aluminium profiles. The drift voltage (-2.1 kV) is applied to an aluminium-coated 50 μm mylar foil which is glued on the radiator unit (see Chapter 3). The radiator unit itself is glued into the drift box and adds mechanical stability to the detector module. It provides gas tightness of the drift volume and keeps the deformation of the drift electrode within the specification ($<$1 mm at an overpressure of 1 mbar).

The drift field is terminated by a plane of cathode wires which is attached to the upper rim of the drift box. It is followed by a plane of anode wires, providing the necessary gas amplification. In this scheme, the wire tension is transferred to the drift box, causing no mechanical stress on the readout plane.

To avoid drift field distortions at the edges of the readout chamber, potential strips are running along the inner wall of the drift box. The strip pattern is etched into a printed circuit board (Fig. 4.7). The potential of each of the strips has been chosen to minimize field distortions. The appropriate voltage to the potential strips is supplied by a voltage divider resistor chain (Fig. 4.7). The value of the last resistor in the chain has been tuned to optimize the electrostatic matching between drift region and amplification region (see Section 4.6).

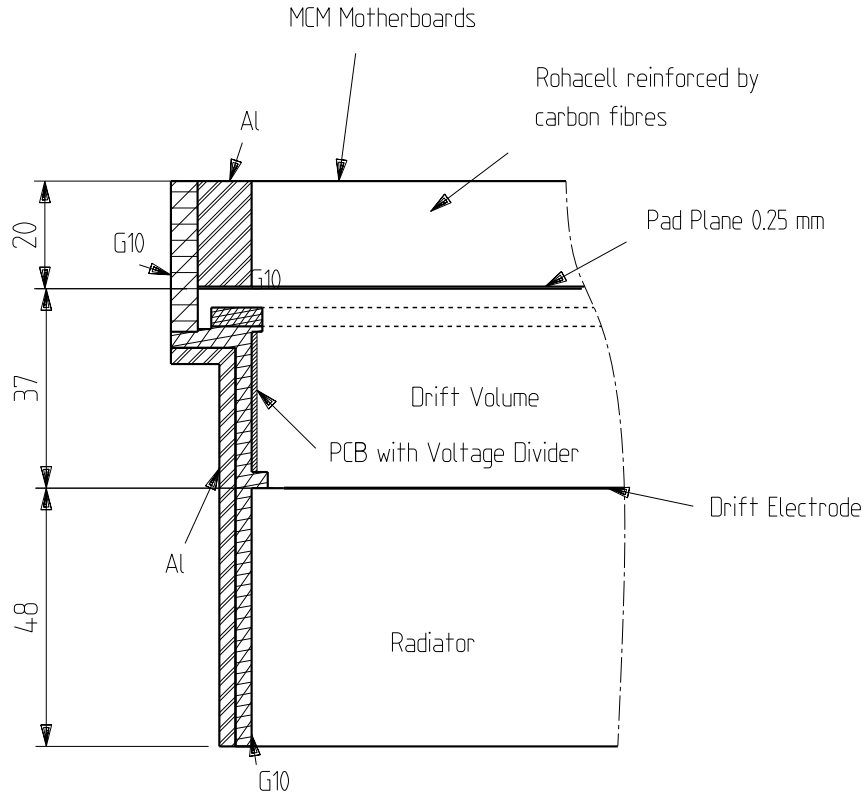

Figure 4.6: Cross section through a TRD detector module.

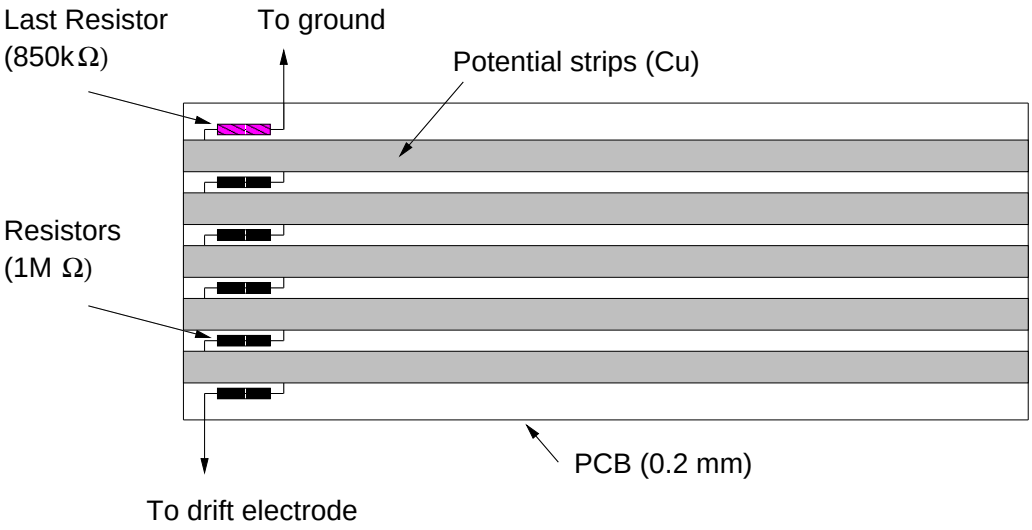

Figure 4.7: Potential strip PCB and voltage divider chain.

The current of the backdrifting positive ions (≈ 0.5 μA per readout chamber, see Section 4.6) could potentially cause a modification of the voltage settings on the potential strips and the drift electrode. The total resistance of 5.85 MΩ from drift electrode to ground potential leads to a chain current of 360 μA at a drift voltage of -2.1 kV. This is sufficiently large to avoid significant ion-induced changes of the drift voltage settings. The power dissipation in the resistor chain is negligible (≈ 1 W).

The readout plane is a composite structure containing the pad plane, a layer of carbon fibre reinforced Rohacell® foam and the Multi Chip Module (MCM) motherboards which carry the front-end part of

the readout electronics (Fig. 4.8). The pad plane is made up of three individual printed circuit boards (2 layers, 0.25 mm), carrying the readout pad pattern at the inside of the detector. Charge signals induced on the pads are passed via plated-through connections to the back side of the pad plane. Flexible cables are soldered to the back side of the pad plane and transmit the analog signals to the MCMs which are mounted on the MCM motherboards (4 layers, 0.4 mm). These motherboards carry a ground plane, voltage and clock distributions and the digital signals.

The mechanical rigidity of the readout plane against gravitational forces and pressure gradients is provided by a 20 mm layer of Rohacell® foam. It is glued to the back side of the pad plane PCBs and guarantees the flatness of the pad surface. It also covers the plated-through holes and the joints between the individual pad plane PCBs to ensure gas tightness. For mechanical rigidity the back side of the Rohacell® foam is covered with a thin carbon fibre laminate, thus forming a sandwich-like structure. Optionally, also thin carbon fibre rods (2 mm diameter) can be used. Prototype measurements and calculations have indicated that the maximum deformation of the pad plane can be kept below 150 μm at the maximum overpressure of 1 mbar if the Rohacell® foam is laminated with a 200 μm carbon fibre layer.

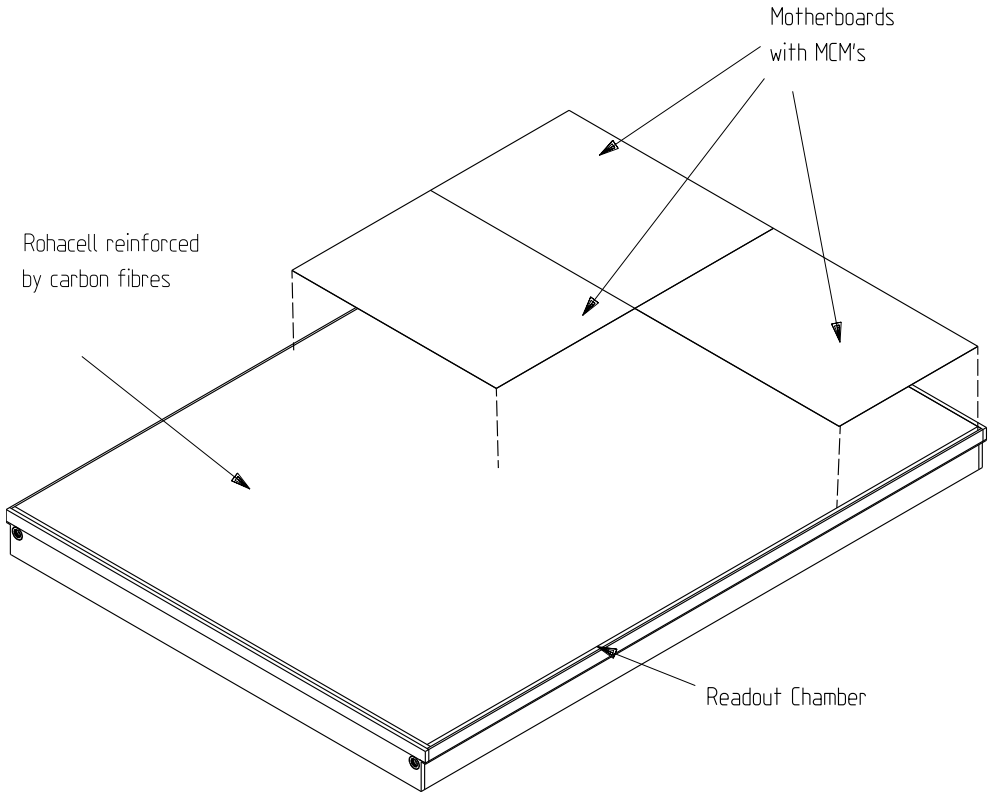

Figure 4.8: Top view of a TRD readout chamber.

4.3 Wire planes

The number of electrons liberated by the passage of a charged particle in the ALICE TRD (275 per cm for a minimum ionizing particle) is not sufficient to produce a measurable signal without further amplification. The readout chambers therefore employ a scheme of two planes of wires, both running in azimuthal direction. They provide gas amplification in the range of 10^4 by avalanche creation. At this gas gain we expect a chamber current of 1 μA/m^2, resulting in a total charge accumulation of 50 μC per year and per cm of wire. For these low doses, we do not expect particular problems with ageing [7], provided proper gas purity and choice of detector materials.

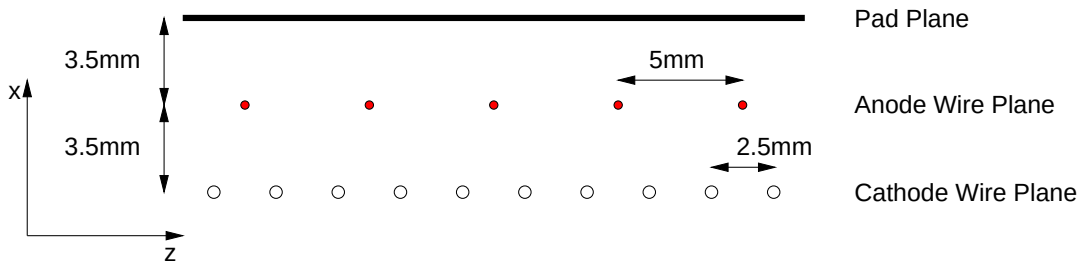

Figure 4.9: Wire geometry of the ALICE TRD readout chambers.

The drift and amplification region are separated by the cathode wire plane (Fig. 4.9). The cathode wires are kept at the same potential as the pad plane (ground). Electrons produced in the drift volume pass the cathode grid and start an avalanche close to the anode wires, which are biased by a positive potential (typically +1.4 kV, see Section 4.6).

The anode wire plane is centered between pad plane and cathode wire plane, with a gap of 3.5 mm between anode wires and pad plane. This gap has been optimized to provide appropriate charge sharing between adjacent pads (see Section 4.4). The pitch between anode wires is 5 mm.

The cathode wires are staggered with respect to the anode wires and have a pitch of 2.5 mm (see Fig. 4.9). The cathode wire plane decouples the drift field from the amplification region and thus allows independent adjustment of drift velocity and gas gain (see also Chapter 14). It is more than 99% transparent for electrons, but prevents about 72% of the positive ions produced in the avalanche from drifting back into the drift region (see Section 4.6).

Materials, dimensions, and tension of the wires used in the ALICE TRD are listed in Table 4.1.

Table 4.1: Materials, dimensions, and tension of the wires used in the ALICE TRD readout chambers.

	Anode wires	Cathode wires
Material	Au plated W	Cu/Be
Diameter	20 μm	75 μm
Tension	0.45 N	1.2 N
Length	100 – 120 cm	100 – 120 cm
Total number	140k	280k

4.4 Readout pads

The positive ions created in the avalanche process in the vicinity of the anode wire move towards the surrounding electrodes, inducing a positive signal on the pad plane. A precise determination of the location of the avalanche in azimuth can be obtained if the induced charge is shared among several adjacent readout pads. The measurement of the azimuthal position in each of the 15 time bins allows a determination of the track angle in the rφ-plane in each TRD layer.

The actual sizes and numbers of pads in each of the readout chambers are listed in Table 4.2. We have chosen rectangular pads with average size 7.25×87.5 mm^2 (Fig. 4.10). This results in a pad area of about 6.3 cm^2. In each readout chamber the pads are grouped in rows of 144, running in azimuthal direction. The total number of pad rows in z-direction is 70-76, depending on the layer. The actual size of the pads is constant within a given readout chamber but varies slightly for different detector modules, because of the change of the overall detector module dimensions as function of radius and z (see Chapter 2). The total number of pads is 1 156 032.

Table 4.2: Dimensions that define the active area and pad sizes in different readout chambers. The numbering scheme for the detector modules is described in Chapter 2.

Layer	Module	Width (y)	Length (z)	Pad rows	Pad width w	Pad length l	Area
[0-5]	[0-4]	[cm]	[cm]	#	[cm]	[cm]	[cm^2]
0 (inner)	0	93.6	120.5	16	0.65	7.53	4.90
	1	93.6	120.5	16	0.65	7.53	4.90
	2	93.6	107.0	12	0.65	8.91	5.80
	3	93.6	120.5	16	0.65	7.53	4.90
	4	93.6	120.5	16	0.65	7.53	4.90
1	0	98.1	128.0	16	0.68	8.00	5.45
	1	98.1	128.0	16	0.68	8.00	5.45
	2	98.1	107.0	12	0.68	8.91	6.07
	3	98.1	128.0	16	0.68	8.00	5.45
	4	98.1	128.0	16	0.68	8.00	5.45
2	0	102.5	131.5	16	0.71	8.21	5.85
	1	102.5	135.5	16	0.71	8.46	6.03
	2	102.5	107.0	12	0.71	8.91	6.35
	3	102.5	135.5	16	0.71	8.46	6.03
	4	102.5	131.5	16	0.71	8.21	5.85
3	0	106.9	139.0	16	0.74	8.68	6.45
	1	106.9	143.0	16	0.74	8.93	6.63
	2	106.9	107.0	12	0.74	8.91	6.62
	3	106.9	143.0	16	0.74	8.93	6.63
	4	106.9	139.0	16	0.74	8.68	6.45
4	0	111.4	139.0	14	0.77	9.92	7.68
	1	111.4	150.0	16	0.77	9.37	7.25
	2	111.4	107.0	12	0.77	8.91	6.90
	3	111.4	150.0	16	0.77	9.37	7.25
	4	111.4	139.0	14	0.77	9.92	7.68
5 (outer)	0	115.8	131.5	13	0.80	10.11	8.13
	1	115.8	157.5	16	0.80	9.84	7.92
	2	115.8	107.0	12	0.80	8.91	7.17
	3	115.8	157.5	16	0.80	9.84	7.92
	4	115.8	131.5	13	0.80	10.11	8.13

Other pad sizes and shapes, such as *chevrons* [8] have also been considered during the R&D phase. An appropriate choice of the chevron geometry allows to adjust the shape of the pad response function over a wide range of pad widths and anode-pad distances (for an overview see Chapter 14). However, chevron pads require high precision during manufacturing of the pad plane and positioning of the anode wires. In addition, chevron pads compared to rectangular pads give rise to a higher pad-to-pad capacitance and thus larger signal cross-talk. Since we found a good solution to achieve the required charge sharing also with rectangular pads and a reasonable wire plane separation, chevron pads are not part of the baseline design presented here.

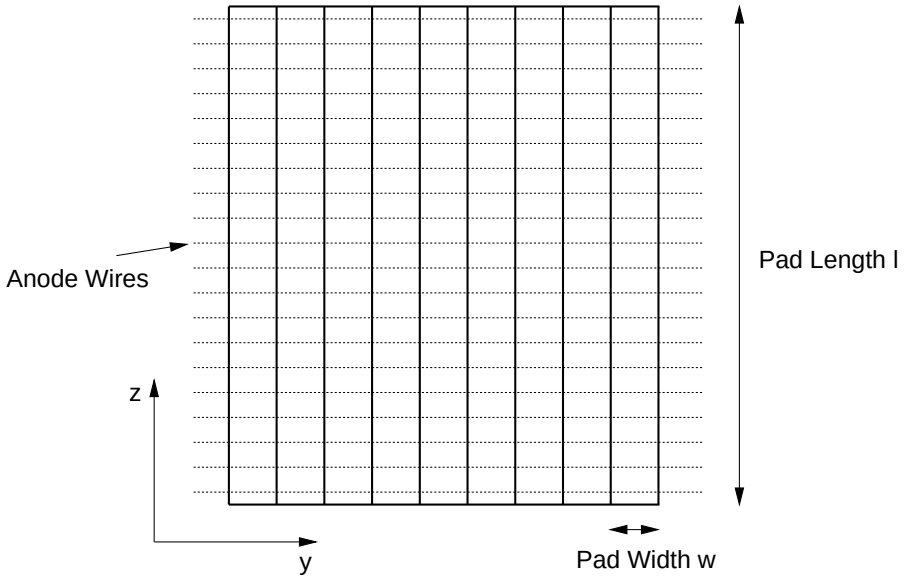

Figure 4.10: Pad geometry of the TRD readout chambers. Also shown are the anode wires.

4.4.1 Pad response function

To achieve the best possible position resolution in azimuthal direction, the induced charge distribution needs to be shared by typically two or three adjacent pads. If more than three pads fire, the resolution suffers from a poorer signal-to-noise ratio, connected with an overall increase of the data volume and a limitation of the two-track separation. Therefore, a proper matching of the pad width w to the width of the induced charge distribution is required. The relative pulse height distribution on adjacent pads, induced by a point-like avalanche at the anode wire, is called the pad response function (PRF) [7]. It can be calculated by integration of the induced charge distribution over the pad area S:

$$\mathrm{PRF}(x,y) = \int_S Q(x',y')\mathrm{d}S. \tag{4.5}$$

The two-dimensional induced charge distribution $Q(x',y')$ depends on the wire geometry and was calculated according to [9]. Figure 4.11 shows the calculated pad response functions for a distance of $h = 3.5$ mm between the pad plane and the anode wire plane. For the range of pad widths in the ALICE TRD (see Table 4.2), the resulting PRFs are approximately Gaussian and a reasonable charge sharing can be achieved.

4.4.2 Improvement of z-resolution

In the present pad design, the coordinate φ_i of a reconstructed point i is directly related to its center of gravity $\langle y_{\mathrm{pad}} \rangle$ in pad space, while the z-resolution is limited by the finite length l of the pads in a given pad row:

$$\varphi_i = \varphi(\langle y_{\mathrm{pad}} \rangle), \tag{4.6}$$

$$z_{\mathrm{row}} - \frac{l}{2} < z_i < z_{\mathrm{row}} + \frac{l}{2}, \tag{4.7}$$

z_{row} being the z-coordinate of the center of a pad row.

Optionally, we consider to tilt the pads slightly by an angle α with respect to the z-axis. If this tilt is performed in opposite direction in consecutive layers of the TRD (Fig. 4.12), significant improvement of the z-resolution can be achieved.

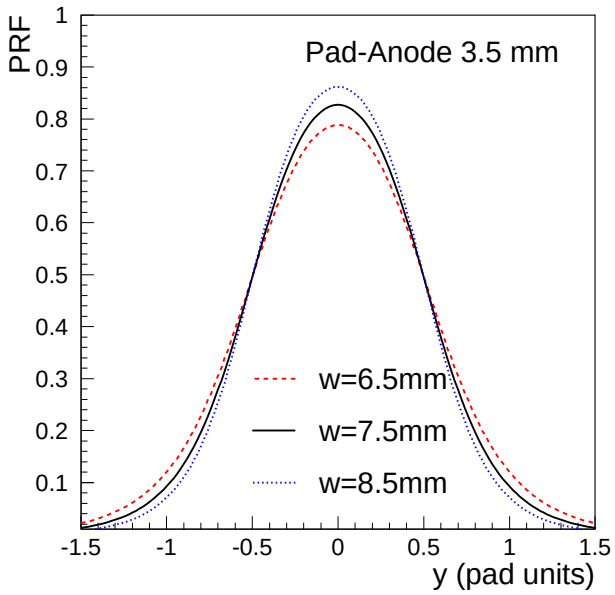

Figure 4.11: PRF for different pad widths.

In the case of tilted pads, the coordinates (φ_i, z_i) of a reconstructed point in a given layer are related to $\langle y_{\text{pad}} \rangle$ and the tilt angle α:

$$\varphi_i = \varphi(\langle y_{\text{pad}} \rangle) + (z_i - z_{\text{row}}) \sin\alpha. \tag{4.8}$$

This way, the measurements of φ_i and z_i in a single layer are no longer independent. However, if the next layer is tilted by -α the point coordinates are given by:

$$\varphi_j = \varphi(\langle y_{\text{pad}} \rangle) - (z_j - z_{\text{row}}) \sin\alpha. \tag{4.9}$$

By matching track points from different layers and assuming an appropriate track model (helix), the best z-position can be determined by a minimization procedure.

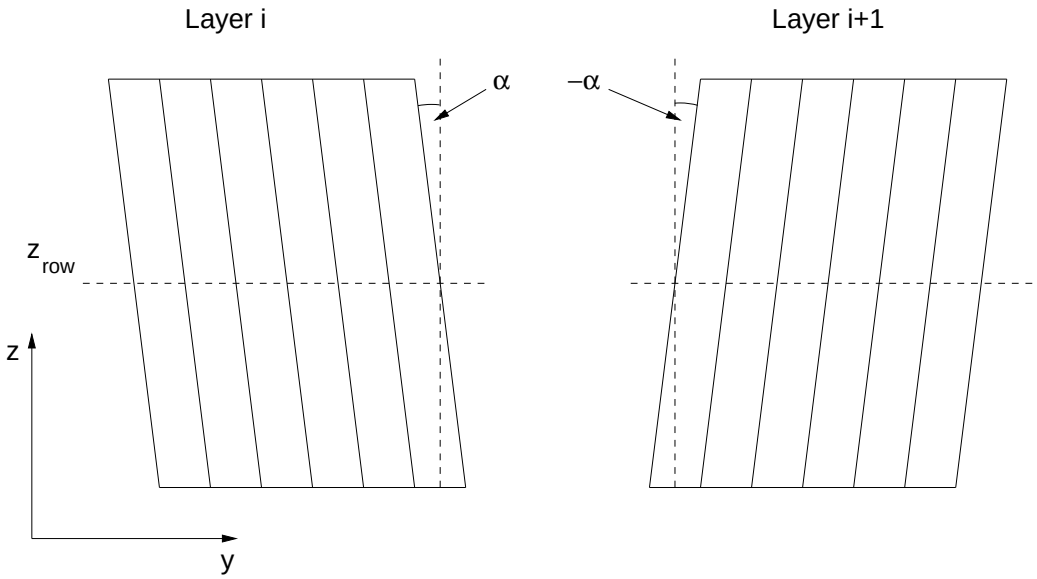

Figure 4.12: Geometry of tilted pads.

We have simulated the φ- and *z*-resolution as function of the pad tilt angle α. For simplicity, we considered only two layers and straight tracks with θ=90°. In that case, the track model is very simple (φ=const., *z*=const.). Figure 4.13 shows the resolution in φ- and *z*-direction as function of the pad tilt angle α. The numbers correspond to the averaged φ- and *z*-positions of the track, using 10 points in each of the two layers. As expected, the resolutions scale with α:

$$r\Delta\varphi \propto 1/\cos\alpha, \tag{4.10}$$

$$\Delta z \propto 1/\sin\alpha, \tag{4.11}$$

as indicated by the dashed lines in Fig. 4.13. Obviously, already at tilt angles around 5° the *z*-resolution can be substantially improved without a noticeable loss in φ-resolution. Note that for individual points the *z*-resolution is limited by the anode wire pitch (5 mm).

Since the impact of tilted pads on the trigger scheme and the offline reconstruction is not yet fully explored they are not part of the baseline design presented here.

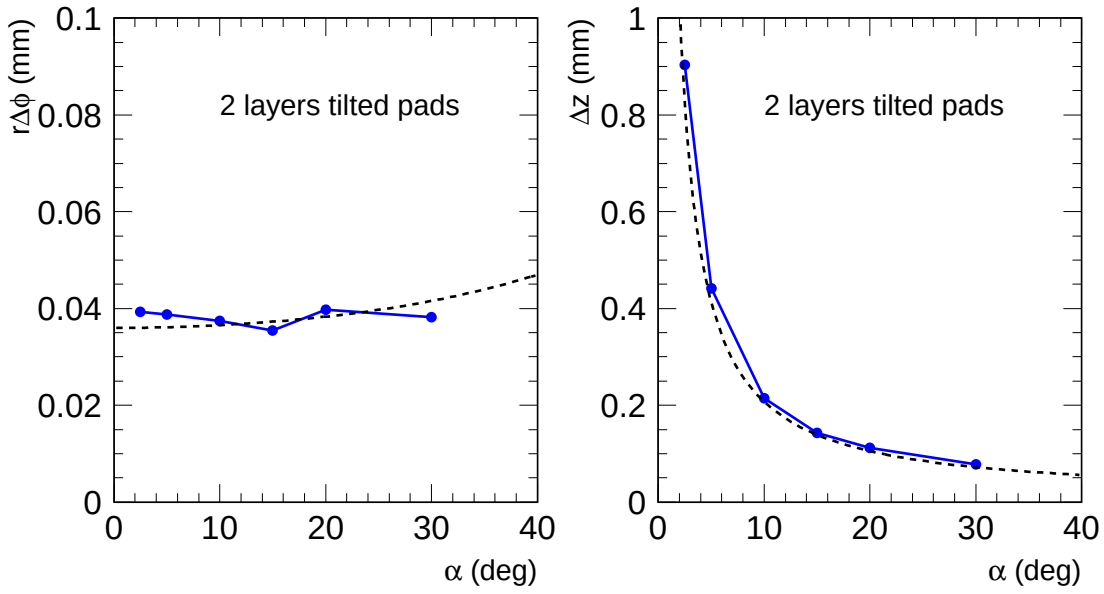

Figure 4.13: Resolution of track averaged φ- and *z*-positions as function of the pad tilt angle α (see text). Two layers with tilt angle ±α are assumed.

4.5 Track reconstruction

Charged particles leave a trace of ionization in the drift volume. The momentum of a particle can be determined by the measurement of the deflection angle of the particle track in the *r*φ-plane. By sampling the time distribution of the arriving electrons in 15 time bins, a set of individual *r*,φ measurements for each track segment can be obtained. Given precise knowledge of the drift velocity, the *r*-coordinate of each point is given by the arrival time. The φ-coordinate can be derived from the distribution of the induced charge over two or three adjacent pads in each time bin.

The charge signal induced on the pad plane is that of the positive ions created in the avalanche process drifting away from the anode wire. Due to the very low mobility of Xe ions (0.57 cm^2/Vs) the induced signal on the pads of a point-like primary electron cluster has a considerable tail (see Fig. 4.14, upper panel). After pulse shaping (shaping time 125 ns FWHM) the signal has a width of approximately 200 ns. However, because of the ion tail the time response function (TRF) is non-Gaussian (see Fig. 4.14, lower panel).

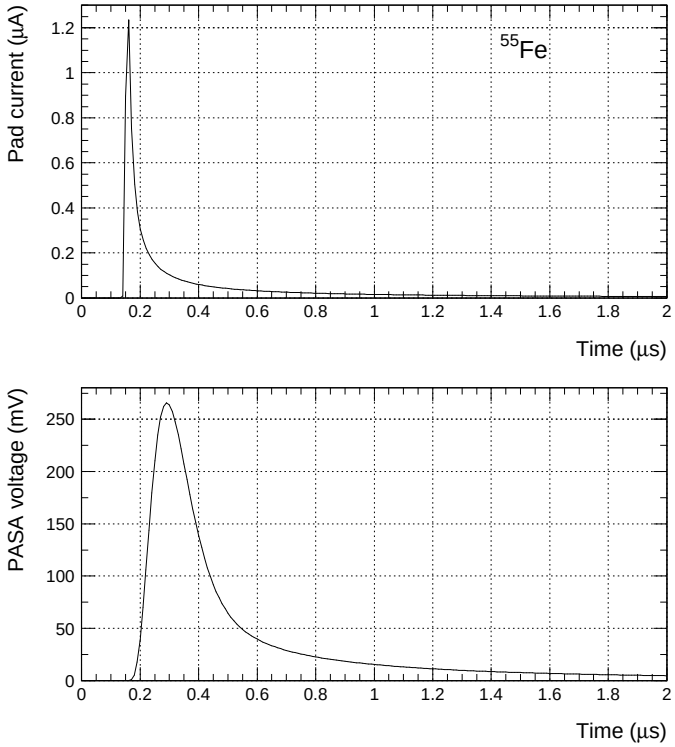

Figure 4.14: Simulated response to a ^{55}Fe signal. Upper panel: the current induced on the readout pads. Lower panel: electronics response after pulse shaping (TRF).

Since the tail of the TRF is long compared to the distance of time bins (133 ns) it leads to a significant correlation among consecutive time bins. If a large charge deposition occurs due to Landau fluctuations or TR absorption on an inclined track, adjacent time bins are 'pulled' away from the trajectory (see Fig. 4.15 for simulated examples).

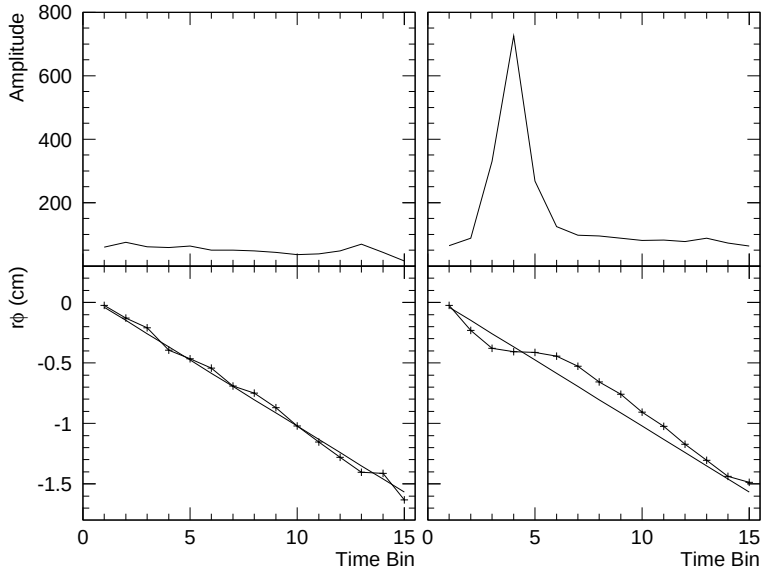

Figure 4.15: Two examples of simulated tracks. In the upper panels the pulse height integrated over neighboring pads is shown; in the lower panels the reconstructed space points (crosses) are compared to the real trajectory (straight line).

This results in a deterioration of the position resolution depending on the incident angle of the track, similar to the well-known $\tan\alpha$-effect in TPCs [7]. This is demonstrated in Fig. 4.16, where the angular resolution was simulated as function of the track angle of incidence relative to the pad plane normal. Note that in the presence of a magnetic field this distribution will be shifted by the Lorentz angle.

One way to reduce this effect is to stretch the time scale of the measurement. This can be achieved by a reduction of the drift velocity. However, a significant increase of the readout time would limit the online trigger capability.

The inclusion of an electronic tail cancellation is under way. Its effect has been demonstrated by applying an offline deconvolution of consecutive time bins to prototype data (see Chapter 14).

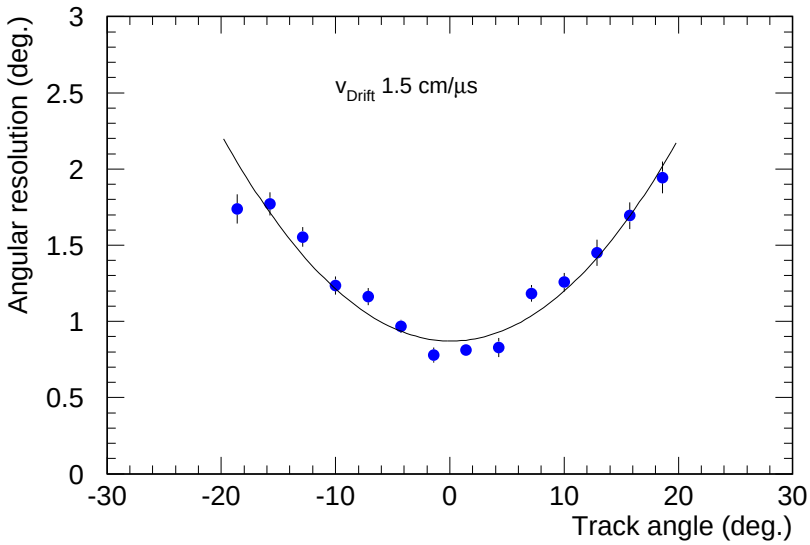

Figure 4.16: Angular resolution as function of the track angle relative to the pad plane normal (B=0).

4.6 Electrostatic calculations

In this section we describe the electrostatic properties for the readout chamber design presented in the previous sections. We determine the operational points and show that the design we have chosen is suited to meet the requirements. All calculations presented here are performed in the framework of the GARFIELD [2] simulation package.

In the calculations, a Xe,CO_2 (15%) gas mixture at atmospheric pressure is assumed. Furthermore, the wire materials, diameters and tensions as listed in Table 4.1 are used.

4.6.1 Gas gain

To achieve a reasonable signal-to-noise ratio we are aiming for a gas amplification of $5{\cdot}10^3$-10^4. The amplification achieved on the anode wire depends on the gas mixture, the pressure, the wire geometry, and the bias voltages. The gas mixture (Xe,CO_2 (15%)) and the operating pressure are mainly determined by other constraints (see Section 4.1 and Chapter 8).

The gas gain as function of the anode wire voltage is shown in Fig. 4.17. The result for our baseline design with an anode-cathode distance of $h = 3.5$ mm and staggered wire planes is compared to a non-staggered wire geometry and to a smaller anode-cathode distance of $h = 2.5$ mm. While there is no noticeable difference between staggered and non-staggered wire planes, the gas gain at a given voltage is larger by almost a factor 5 in the case of $h = 2.5$ mm. However, the desired sharing of the induced charge

among several adjacent pads requires an anode-cathode separation of $h = 3.5$ mm. For this geometry, we achieve a gas gain of 8000 at an anode voltage $U_a = 1420$ V.

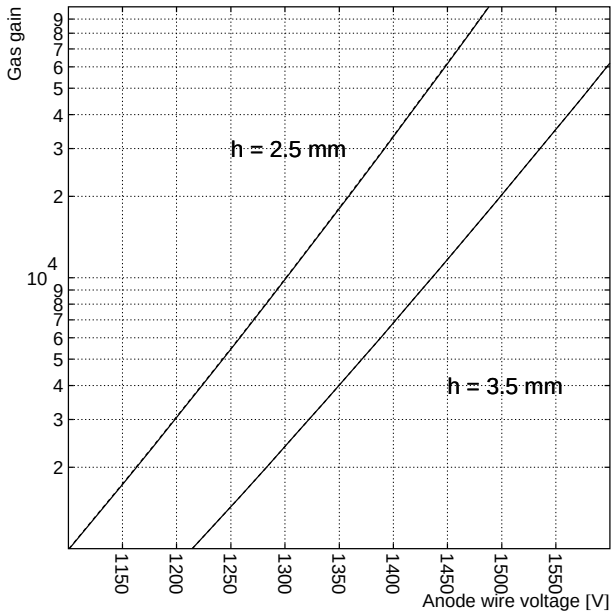

Figure 4.17: Gas gain as function of the anode voltage.

High momentum tracks originating from the main vertex traverse the TRD preferentially under small angles with respect to the wire normal. For a given track, this can lead to a relatively large charge deposition along a limited piece of anode wire. The ions created in the avalanche process build up a cloud of positive charge slowly moving away from the wire. This leads to a reduction of the electric field in the vicinity of the wire and therefore to a lower gas gain for subsequent electrons. As a consequence, the gas amplification decreases as function of the drift time for tracks which cross the TRD under small angles with respect to the wire normal. Following [7] we calculated the gain attenuation for minimum ionizing particles in Xe,CO_2 (15%) . Figure 4.18 shows the pulse height as function of the drift time for different angles of incidence. The pulse height was normalized to that of 17° tracks where the effect is negligible. An attenuation of the gas gain is clearly visible, most pronounced for small track angles. The calculations for a gas gain of 10^4 are consistent with our prototype data (see also Chapter 14). This observation underlines that the TRD readout chambers should be operated at gas gains not exceeding 10^4, in line with the planned values.

4.6.2 Gain stability

The positive voltage applied to the anode wires causes the anode wires to sag towards the pad plane. The sagitta of the sagging anode wire depends on the wire material, diameter, length and tension, the wire geometry, and the applied voltage U_a. For this computation, we use the maximum wire length in the TRD of 120 cm. We show the anode wire sag as function of U_a in Fig. 4.19 (left panel). Again, different wire geometries are compared. The sag is significantly smaller for $h = 3.5$ mm compared to $h = 2.5$ mm. At a typical operating voltage of $U_a = 1400$ V ($h = 3.5$ mm) the anode wire sag is 35 μm. Not shown is the contribution from gravity, which amounts to about ± 20 μm, depending on the orientation of the readout chamber.

Also, the cathode wires are exposed to electrostatic forces. Their sag, however, is small due to the larger tension applied to them (Fig. 4.19 right panel). The impact of the cathode wire sag on the uniformity of the electric drift field is negligible.

The anode wire sag leads to a variation of the gas gain along the wire. The relative gain variation

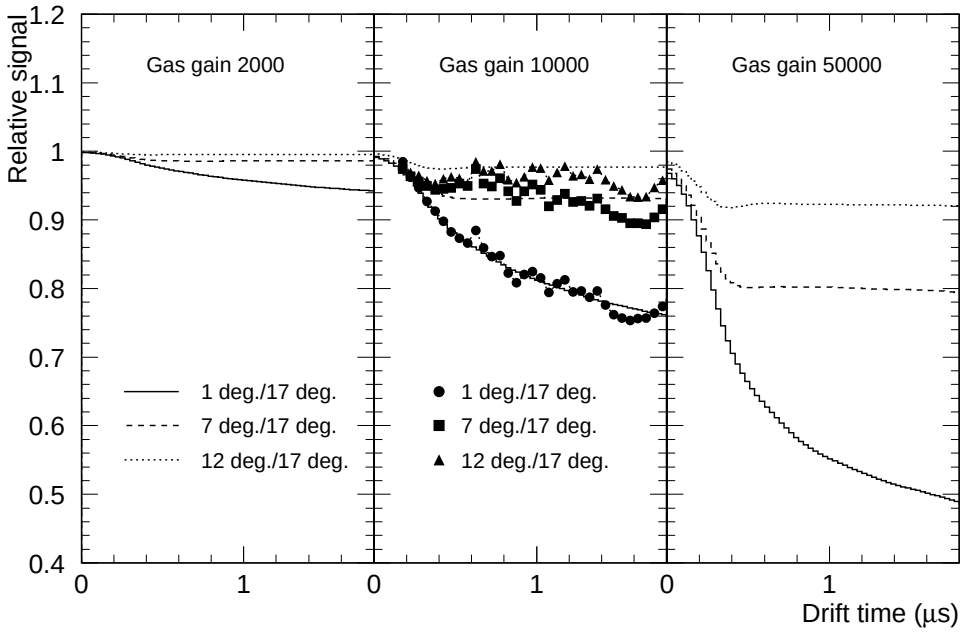

Figure 4.18: Calculated relative gas gain as function of the drift time for different gas gains and angles of incidence. The data points are from prototype measurements (see Chapter 14).

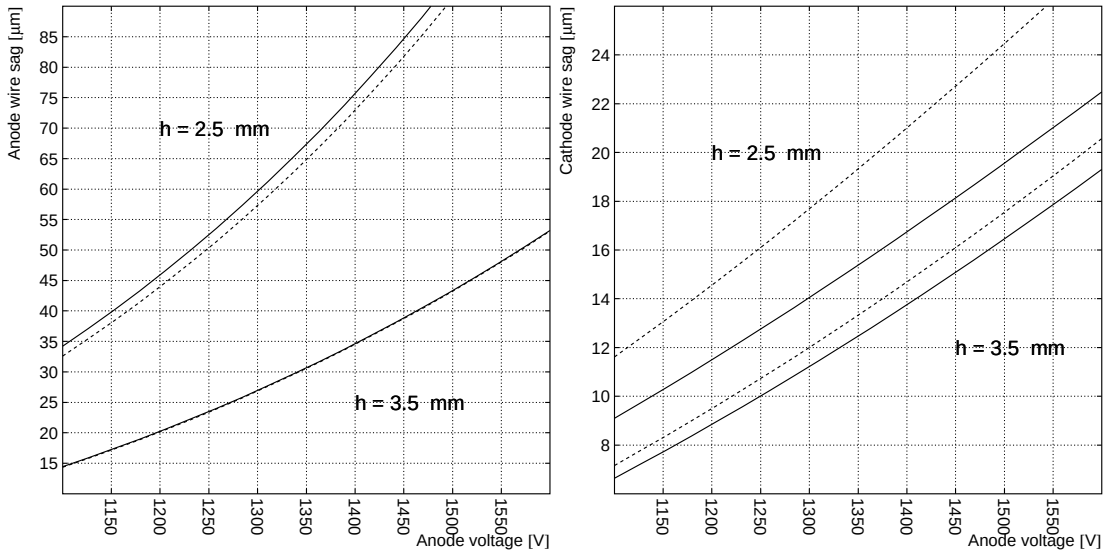

Figure 4.19: Anode wire sag (left) and cathode wire sag (right) as function of the anode voltage. The dashed line refers to the non-staggered geometry.

as function of the sag is computed for $U_a = 1400$ V and shown in Fig. 4.20. At the maximum sag of 35 μm we calculate a relative gain variation ΔGain/Gain$\approx$1.7%. Adding the contribution from gravity we conclude that the gain variations caused by wire sag are below 3% everywhere in the detector, assuming a perfectly flat pad plane.

The operation of the detector at a slight overpressure of 1 mbar leads to a deformation of the pad plane of about 150 μm. From our calculations we expect this to cause a gain variation of 7%. This gain variation is partially compensated by the anode wire sag. The possibility of a minimization of the gain variations by placing the anode wire plane slightly asymmetric between cathode wire plane and pad plane is under investigation.

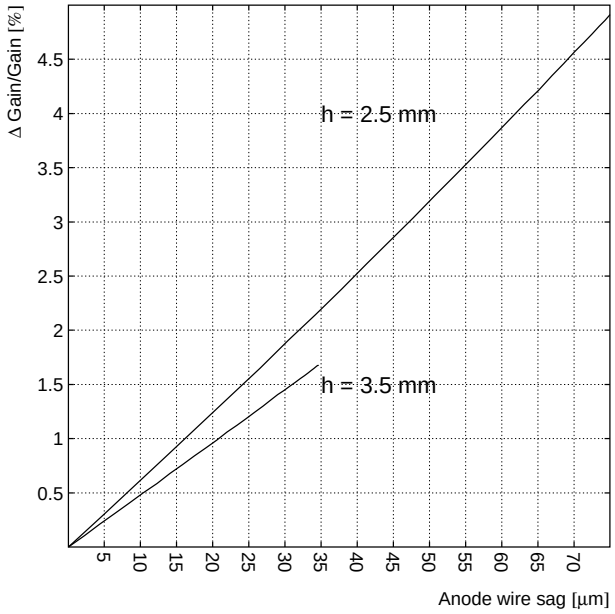

Figure 4.20: Relative gas gain variation as function of the anode wire sag.

4.6.3 Pad coupling

The charge induced by the movement of the positive ions away from the anode wire is shared among all surrounding electrodes. Only a fraction of it couples to the readout pads and contributes to the measured signal. The fraction of the charge which couples to the pads is a function of the ion drift time and direction and therefore depends on the angular distribution of the avalanche. It should be noted that only for gas gains well above 10^4 the avalanche can be assumed to be isotropic around the wire [7].

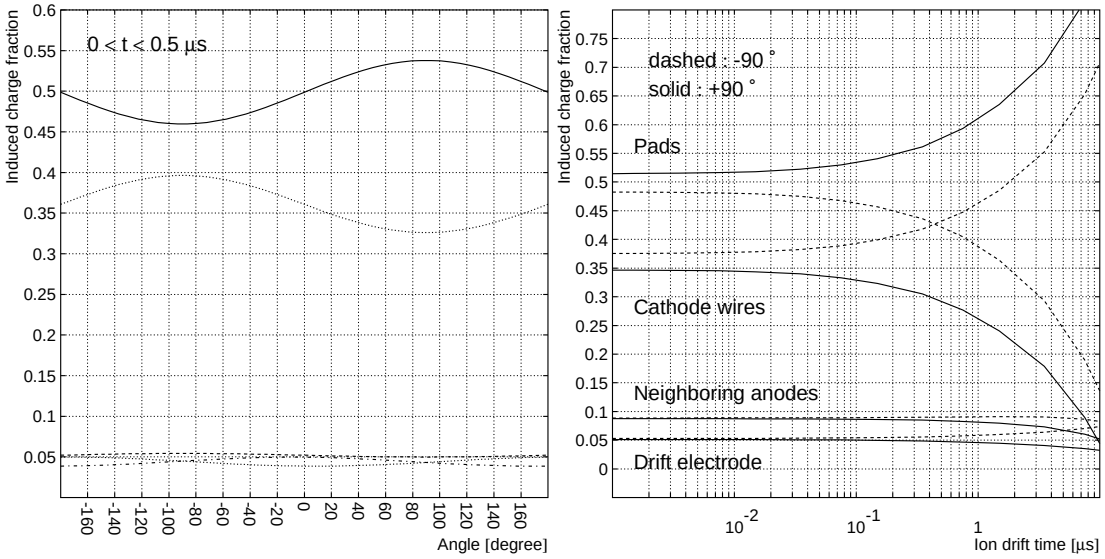

Figure 4.21: Left panel: fractions of charge induced on the various electrodes as a function of the angle under which the ions drift away from the wire. Solid: pads, dotted: cathode wires, dashed: drift electrode, dash-dotted and dotted: neighboring anode wires (left and right). Right panel: ion drift time dependence of the induced charge for 90° (ions drifting towards the pads) and -90° (towards the cathode wires).

Figure 4.21 (left panel) shows the fraction of the induced charge flowing to the various electrodes during the first 500 ns as function of the angle under which the ions leave the anode wire. As expected,

the signal induced on the pads is maximal if the ion drifts into the direction of the pad plane (90°) and minimal if it drifts to the cathode wires (-90°). On average, we expect about 50% of the signal to be induced on the readout pads and 36% on the cathode wires. Note that a significant fraction of the signal is induced on the neighboring anode wires and the drift electrode.

The ion drift time dependence of the induced charge is shown in Fig. 4.21 (right panel) for ions drifting towards the pad plane (90°) and towards the cathode wires (-90°). The fraction of the induced charge on a given electrode is approximately constant over the first 1 μs (note that the typical integration time of the readout eletronics is $<$500 ns, see Fig. 4.14). By that time, the ions have moved away from the anode wire by about 200 μm.

4.6.4 Ion feedback

Unlike many other drift detectors, the readout chambers in the ALICE TRD contain no gating grid. Therefore, all ionization produced in the drift region will inevitably lead to avalanche creation at the anode wires. This causes a continuous current of positive ions drifting back into the drift volume and ending at the drift electrode. However, not all ions find their way back into the drift volume. Figure 4.22 shows the drift lines and lines of equal drift time (isochrony lines) of positive ions produced at the anode wire. Only about 28% of them drift back into the drift volume, the remainder reaches the surrounding electrodes. This leads, under operating conditions, to an ion feedback current of about 0.5 μA through the drift volume (see also Section 4.3). From that we expect a charge density in the drift volume of about $1.6 \cdot 10^5$ ions/cm^3. The resulting distortions of the electric drift field can be calculated and were found to be well below 10^{-3} with respect to the nominal field strength of 700 V/cm.

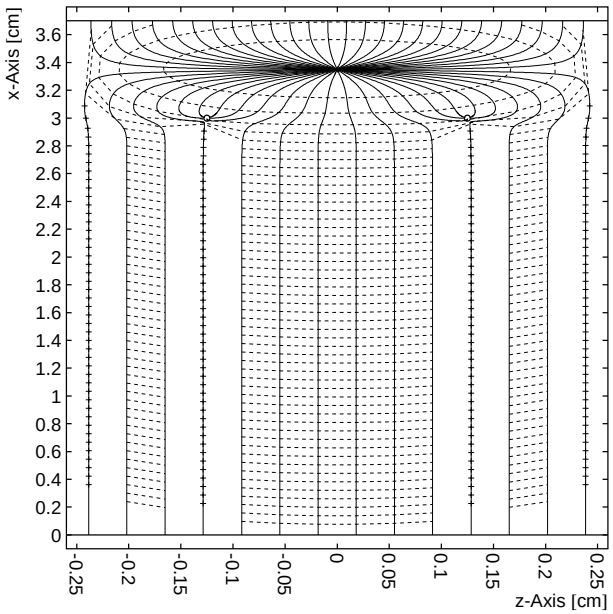

Figure 4.22: Drift lines (solid) and isochrony lines (dashed) of positive ions starting from the anode wire. The anode wire is at z=0 cm, the cathode wires are at $z = \pm 0.125$ cm.

4.6.5 Isochrony

The finite pitch between the wires causes a systematic drift time variation for electrons starting at the same radius, but from different z-positions. In the presence of Landau fluctuations this can potentially lead to a deterioration of the drift time determination. The drift time variation for electrons starting at constant r close to the drift electrode is shown as function of their z-position relative to the anode wire

in Fig. 4.23. We have implemented the observed non-isochrony into a microscopic drift simulation and found no noticable effect on the position resolution.

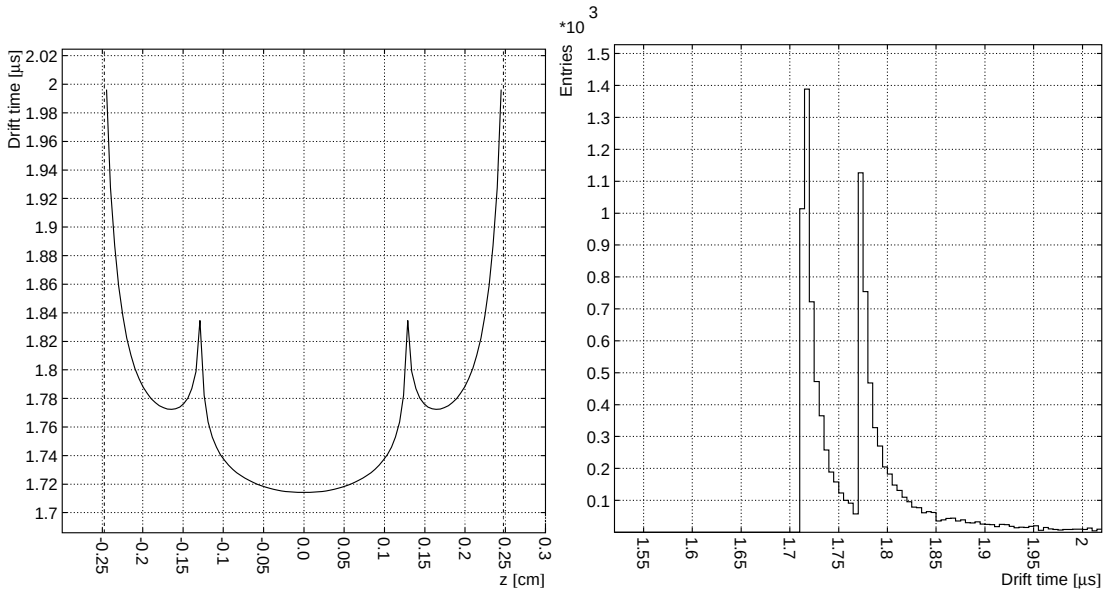

Figure 4.23: Left panel: drift time variation within a drift cell. The anode wire is at z=0 cm, the cathode wires are at $z = \pm 0.125$ cm. Right panel: projection on the time axis. The r.m.s. of the distribution is 71 ns.

4.6.6 Electrostatic matching

Due to the finite pitch of the cathode wires (2.5 mm) not all field lines from the amplification region end on the cathode wires. As a result, the effective ground plane is not at the position of the cathode wires but shifted by about 0.7 mm towards the drift electrode (Fig. 4.24).

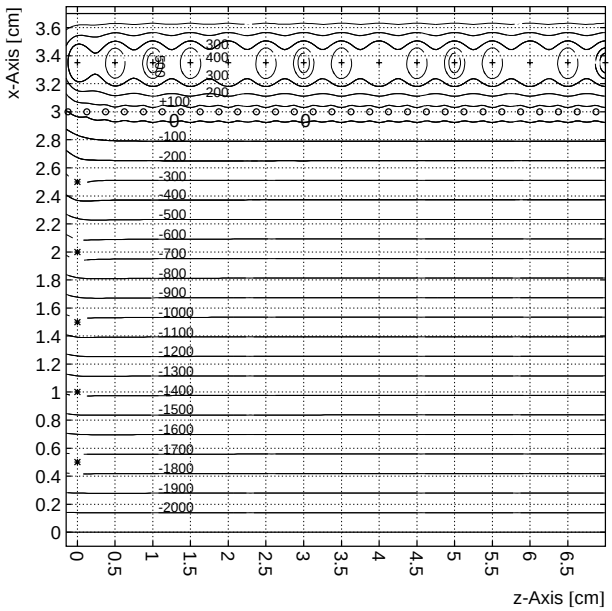

Figure 4.24: Equipotential lines in the readout chambers, using $U_a = 1400$ V and $U_{\text{drift}} = -2100$ V. The positions of the potential strips are indicated by the stars at z=0.

This can be compensated by proper choice of the last resistor in the voltage divider chain (see Section 4.2). Figure 4.25 shows the electric field 5 cm away from the voltage divider and as function of the distance from the drift electrode ($U_a = 1400$ V and $U_{\text{drift}} = -2100$ V). Fixing all other resistors in the chain to 1 MΩ, we obtain the best result for R_{last}=850 kΩ.

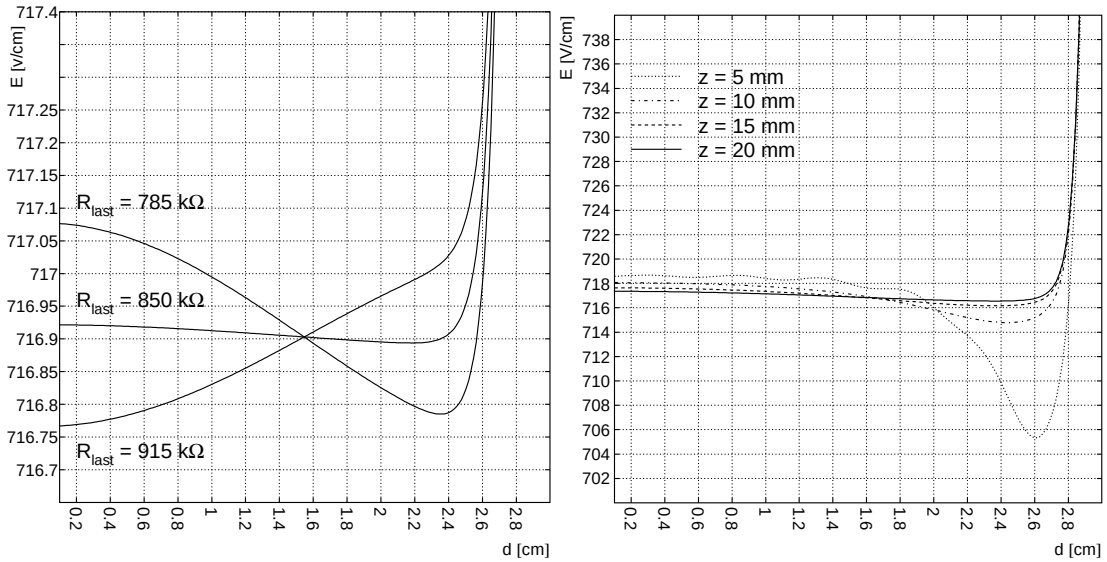

Figure 4.25: Left panel: electric drift field as function of the distance d to the drift elecrode and for different values of R_{last}. The distance z to the potential strips is 5 cm, the voltage settings are $U_a = 1400$ V and $U_{\text{drift}} = -2100$ V. Right panel: same but for several distances z closer to the potential strips and fixing R_{last} to 850 kΩ.

Moving closer to the edge of the drift volume, the granularity of the voltage divider becomes visible, as shown in the right panel of Fig. 4.25. However, only 10 mm away from the potential strips the field becomes smooth and varies by less than 0.5% with respect to its nominal value.